eChem
https://www.sciltp.com/journals/eChem

Article

Bound Water-Mediated Fast Ion Transport in Viscoelastic Solid-State Electrolyte Boosting Performance of Solid-State Zinc-Ion Batteries

Yachen Cao [1], Weijia Lin [1], Lirui Xing [1], Minghui Ye [2], Yufei Zhang [2], Yongchao Tang [2], Xiaoqing Liu [2], Zhipeng Wen [2], Qingyu (Alex) Yan [3], Wencheng Du [1,*] and Chengchao Li [2,*]

[1] School of Advanced Manufacturing, Guangdong University of Technology, Guangdong Provincial Laboratory of Chemistry and Fine Chemical Engineering Jieyang Center, Jieyang 515200, China
[2] Guangdong Provincial Laboratory of Chemistry and Fine Chemical Engineering Jieyang Center, Guangdong Provincial Key Laboratory of Plant Resources Biorefinery, School of Chemical Engineering and Light Industry, Guangdong University of Technology, Guangzhou 510006, China
[3] School of Materials Science and Engineering, Nanyang Technological University, Singapore 637819, Singapore
* Correspondence: duwencheng@gdut.edu.cn (W.D.); licc@gdut.edu.cn (C.L.)

How To Cite: Cao, Y.; Lin, W.; Xing, L.; et al. Bound Water-Mediated Fast Ion Transport in Viscoelastic Solid-State Electrolyte Boosting Performance of Solid-State Zinc-Ion Batteries. *eChem* **2025**, *1*(1), 4. https://doi.org/10.53941/echem.2025.100004.

Received: 12 September 2025
Revised: 16 October 2025
Accepted: 18 October 2025
Published: 3 November 2025

Abstract: Efficient ion transport represents a key challenge in the development of solid-state zinc-ion electrolytes. While the introduction of bound water is known to enhance ionic conductivity, the regulation of its content and its precise role in the ion transport mechanism remain inadequately understood. Herein, we systematically investigate the role of water content (0–19.87 wt%) in a poly(ethylene glycol) (PEG)-based viscoelastic solid-state electrolyte (V-SSE) in modulating Zn^{2+} transport and enhancing the performance of Zn||I_2 batteries. Through positron annihilation lifetime spectroscopy, Fourier transform infrared spectroscopy, and molecular dynamics simulations, we observe that the free volume expands from 152 Å^3 to 163 Å^3 with increasing water content up to 9.16%, facilitating ion mobility. Beyond this level, free volume slightly decreases, yet ionic conductivity continues to rise, suggesting alternative promoting mechanisms. At a critical H_2O-to-ether oxygen (EO) molar ratio of 1:1, a threefold increase in the ion diffusion coefficient occurs compared to that at H_2O:EO = 1:3, stemming from shortened transport distance and enhanced diffusion kinetics. Consequently, the bound water-mediated V-SSE enables a high specific capacity of 170–208 mAh g^{-1} in Zn||I_2 full cells, approximately twice that of the anhydrous system (94 mAh g^{-1}), and maintains stable cycling over 3000 cycles. This study elucidates the multirole mechanism of bound water in enhancing ion conduction without compromising electrochemical stability, providing valuable insights for the design of high-performance solid-state electrolytes.

Keywords: solid-state zinc-ion batteries; fast ion transfer; bound water mediation; enlarged free volume; shortened transport distance

1. Introduction

Ionic transport in solid materials is a critical determinant of the performance and practical viability of rechargeable solid-state metal-ion batteries [1–4]. With the escalating demands from electric vehicles, portable electronics, and grid-scale energy storage systems for higher energy density, improved safety, and extended cycle life, conventional liquid electrolytes are increasingly constrained by inherent limitations such as leakage, flammability, and dendrite formation. Solid-state batteries have emerged as a leading candidate for next-generation

energy storage technologies, benefiting from their intrinsic safety, wider electrochemical windows, and potential compatibility with high-capacity electrode materials [5–7]. Nevertheless, the overall performance of solid-state batteries is strongly governed by the ion transport kinetics within both the solid electrolyte and electrode materials. Specifically, the ionic conductivity of the solid electrolyte directly dictates the power density and charge–discharge efficiency of the cell. For example, most currently developed solid polymer electrolyte systems exhibit limited ionic conductivity, typically below 10^{-3} S/cm [8–11], which restricts cycling to low current densities (<0.1 A/g) and compromises capacity retention and high-rate performance. Although various strategies, including crystal phase engineering and the incorporation of nanoscale fillers, have been explored to synergistically enhance ion transport pathways [12–18], the achieved levels of ionic conductivity and interfacial stability still fall short of practical application requirements.

The sluggish migration of ions in polymer-based solid electrolytes, particularly multivalent metal ions, originates from strong Coulombic interactions between the metal ions and the polymer matrix, restricted chain mobility, and limited free volume. Such limitations are often intensified by the presence of high crystallinity and long-chain structures, which collectively hinder efficient ion transport [19–22]. Owing to their high charge density and strong polarizing nature, multivalent ions (e.g., Mg^{2+}, Zn^{2+}, Al^{3+}) tend to form stable coordination bonds with ligand groups in the electrolyte, substantially elevating the energy barriers for intra- and interchain migration. For example, in organic polymer electrolytes such as those based on poly(ethylene oxide), multivalent ions preferentially coordinate with ether oxygen groups, which not only impedes ion dissociation but also restrains the segmental motion of polymer chains that is essential for ion hopping. These pronounced interactions result in low ionic conductivity often below 10^{-4} S/cm, and aggravate space-charge polarization at solid–solid interfaces. Such effects contribute to uneven local ion concentration gradients, increased interfacial impedance, and accelerated capacity fade during cycling [23,24].

In recent years, structural optimization strategies such as promoting amorphization or designing high-dielectric matrices have been explored to weaken ion–matrix interactions in solid electrolytes. Despite these efforts, the resulting ion transport kinetics remain unsatisfactory [25–31], and overall performance continues to fall considerably short of that achieved by conventional liquid electrolytes, thereby hindering practical implementation. The introduction of salt–oligomer systems with weakly coordinating moieties has led to markedly improved ion mobility compared to long-chain polymer analogues. However, their ionic conductivity at room temperature remains substantially lower than that of liquid electrolytes [32–34], and the inherent liquidity of oligomers at ambient conditions undermines the mechanical integrity required for freestanding solid electrolytes.

To overcome sluggish ion transport in solid-state systems, we recently developed a viscoelastic solid electrolyte with easily adjustable viscoelasticity based on a dynamic weak-bonding framework incorporating a limited amount of bound water [35]. This system achieves high ionic conductivity, up to 10^{-3} S/cm, approaching the performance level of liquid electrolytes. Nevertheless, the mechanistic role of water in facilitating multivalent-ion transport within such a framework is still not well defined. Key questions, such as how water molecules influence free volume and ion transport kinetics, have yet to be clearly addressed. Thus, a systematic investigation into the interplay between bound water and ion transport is crucial, both for advancing fundamental understanding and for guiding the design of high-performance solid electrolytes.

In this study, we adopt a poly(ethylene glycol) (PEG)-based viscoelastic solid-state electrolyte (V-SSE) as a model platform to systematically examine the influence of bound water content (ranging from 0 to 19.87 wt%) on Zn^{2+} transport behavior and to unravel the underlying mechanism of bound water-facilitated ion migration. We first assessed how water content modulates key electrochemical characteristics, including the electrochemical stability window and ionic conductivity. Subsequent physicochemical characterization and theoretical simulations allowed us to probe the role of water molecules in tuning free volume and ion diffusion kinetics. Our results reveal that moderate water content enlarges free volume, while excess water leads to its contraction. Notably, ionic conductivity increases monotonically with water content, suggesting the involvement of factors beyond free volume alone. Further analysis identified the molar ratio of water to ether oxygen (EO) units in PEG as a critical governing parameter. At a threshold H_2O:EO ratio of 1:1, the Zn^{2+} diffusion coefficient increases threefold compared to that at H_2O:EO = 1:3, attributed to shortened ion transport distances and lowered energy barriers. In full-cell Zn||I_2 tests, the bound water-mediated V-SSE enabled substantially enhanced capacity, with the optimized electrolyte delivering a high specific capacity of 170–208 mAh g^{-1}—nearly double that of the anhydrous analogue (94 mAh g^{-1}). It also maintains stable cycling for over 3000 cycles. This study offers fundamental insights into the role of bound water in boosting ionic conductivity while maintaining electrochemical stability, thereby providing a rational design strategy for high-performance solid-state electrolytes.

2. Materials and Methods

2.1. Preparation of V-SSE

All chemicals and materials used in this study were commercially sourced (Shanghai Macklin Biochemical Technology Co., Ltd, Shanghai, China) and are characterized by their low cost and high safety. In a typical synthesis, 1.5138 g of zinc trifluoromethanesulfonate was dissolved in varying amounts of water (0, 0.4303, 0.6158, 1.1890, and 1.5159 g, respectively) together with 3.0400 g of poly(ethylene glycol) 400 (PEG400). Subsequently, 1.5200 g of nano-SiO_2 (15 nm) was introduced, and the mixture was stirred until a homogeneous dough-like solid formed. The resulting composite was kneaded thoroughly and allowed to rest overnight. The final V-SSE bulk material could be readily pressed into thin films under mild pressure (<0.1 MPa).

2.2. Preparation of I_2/AC Composite

The iodine/activated carbon (AC) composite was prepared as follows. Elemental iodine (0.8292 g, Macklin Shanghai, China) was placed in an agate mortar, followed by the addition of 10 mL of ethanol and 0.7030 g of AC (Jiangsu XFNANO Materials Tech Co., Ltd, Nanjing, China). The mixture was thoroughly ground to achieve homogeneity, after which 10 mL of water was introduced, and grinding was continued to form a uniform slurry. The slurry was transferred to a glass culture dish and dried overnight under ambient conditions. The resulting solid was further heated at 60 °C for 2 h in an oven to stabilize the composite structure. The final product, an iodine/AC composite, was obtained, and its iodine content was determined gravimetrically to be 50.18 wt%.

2.3. Preparation of I_2 Electrode Slice

The I_2/AC composite-based cathode was typically prepared by thoroughly mixing 80.0 mg of I_2/AC composite, 10.0 mg of zinc trifluoromethanesulfonate (Macklin, Shanghai, China), 10.0 mg of carbon black (RHAWN, Shanghai, China), and 30.0 mg of glycerol-based random polyether (Shandong Yousuo, Linyi, China). The mixture was ground continuously to ensure complete homogenization, during which it gradually transformed into a viscous slurry. This slurry was then uniformly coated onto carbon paper discs (1 cm in diameter). The areal iodine loading on the carbon paper was precisely controlled between 1 and 2 mg cm^{-2}.

2.4. Material Characterization

LF-NMR relaxation measurements were performed on a MacroMR12-60 nuclear magnetic resonance analyzer (Suzhou Niumag Analytical Instrument Co., Ltd., Suzhou, China) operating at a resonance frequency for protons of 12 MHz. The magnetic field strength was 0.5 T permanent, and the radio frequency diameter was 25 mm, with 90° (P1) and 180° (P2) pulse times of 7.4 μs and 11.6 μs, respectively. The echo time was 0.08 ms and the number of echoes was 500. The relaxation signals were collected by NMR Analysis software and Carr–Purcell–Meiboom–Gill (CPMG) pulse sequences. Positron annihilation lifetime measurements were performed utilizing a fast-fast coincidence circuit in conjunction with scintillation detectors, which offered a time resolution of 0.180 ns. The positron source is 22 Na (20 μCi). Time dispersion of the multi-channel analyzer was 20 ps/channel. High-magnification morphologies and EDS mapping were conducted on a scanning electron microscope (Oxford instrument). Time-of-Flight Secondary Ion Mass Spectrometer (TOF-SIMS) was conducted on a TOF-SIMS 5 iontof instrument. Attenuated total reflectance-Fourier transform infrared spectroscopy (ATR-FTIR) spectra were recorded on a Fourier transform infrared spectrometer (Thermo Scientific Nicolet In10, Thermo Fisher Scientific, Waltham, MA, USA). Raman spectroscopy was carried out in a Raman spectrometer (HORIBA HR Evolution, Kyoto, Japan) with a 1064 nm laser. The scans were performed in the region of 3700–100 cm^{-1}.

2.5. Electrochemical Measurements

Electrochemical measurements, including linear scanning voltammetry (LSV) and electrochemical impedance spectroscopy (EIS), were performed using an advanced electrochemical workstation (DyneChem). Additionally, voltage-time curves of symmetric cells were systematically evaluated using the NEWARE Battery Test System (Model CT-4008Tn-5V10mA-HWX, Shenzhen, China), a highly reliable testing platform designed for precise battery characterization.

The ionic conductivity of V-SSE was measured by the EIS method. The frequency and voltage amplitude were 10^5–0.1 Hz and 10 mV, respectively. The ionic conductivity (σ) is calculated by the following equation:

$$\sigma = \frac{l}{R \times S}$$

where l is the thickness, R is the resistance, and S is the tested area.

For the symmetric cell cycling tests, CR2025-type coin cells were assembled using two identical zinc foil anodes (~17 μm thickness) separated by a V-SSE film (~100 mg). Zinc–I_2 full cells were constructed in a two-electrode configuration, with zinc foil (~17 μm) as the anode, the I_2 electrode slice as the cathode, and the V-SSE film as the solid electrolyte. All cycling tests were carried out using a Neware battery test system under various current densities.

2.6. Molecular Dynamics Simulation

Classic molecular dynamics simulations were carried out to investigate the mixed system at the atomic level. Two Bulk cases (A: H_2O:EO = 1:3, B: H_2O:EO = 1:1) were built for Molecular Dynamics simulations.

Case A contains 50 PEG, 27 $Zn(OTF)_2$, 150 H_2O molecules. Case B contains 50 PEG, 27 $Zn(OTF)_2$, 450 H_2O molecules. The initial configuration systems were constructed through the software of PACKMOL [36], and all the molecules were randomly inserted in a cubic simulation box.

The OPLSAA force field was employed to describe the molecules [37]. CM5 charge integrated in AuToFF web server. The molecular force field is consisted of nonbonded and bonded interaction. The nonbonded interaction contains van deer Waals (vdW) and electrostatic interaction, which is described by the Equation (1) and Equation (2), respectively.

$$E_{LJ}(r_{ij}) = 4\varepsilon_{ij}\left(\left(\frac{\sigma_{ij}}{r_{ij}}\right)^{12} - \left(\frac{\sigma_{ij}}{r_{ij}}\right)^{6}\right) \quad (1)$$

$$E_c\left(r_{ij}\right) = \frac{q_i q_j}{4\pi\varepsilon_o\varepsilon_r r_{ij}} \quad (2)$$

In the equation, q_i and q_j are the atomic charge, r_{ij} is the distance between atoms, σ is the atomic diameter, ε is the atomic energy parameter.

For different kinds of atoms, the geometric mix rules were adopted for vdW interactions, which follows Equation (3). The cutoff distance of vdW and electronic interactions was set to 1.2 nm, and the PME method was employed to calculate long-range electrostatic interactions.

$$\sigma_{ij} = \left(\sigma_{ii} * \sigma_{jj}\right)^{\frac{1}{2}}; \varepsilon_{ij} = \left(\varepsilon_{ii} * \varepsilon_{jj}\right)^{\frac{1}{2}} \quad (3)$$

For the simulation, an energy minimization was first employed to relax the simulation box. Then, an isothermal-isobaric (NPT) ensemble with a 1.0 fs time step is employed to optimize the simulation box, where the temperature is set to 298.15 K and the pressure is set to 1.0 atm. The temperature and pressure are kept via the Nose-Hoover thermostat and Parrinello-Rahman barostat, respectively. The NPT optimization time was set to 12.0 ns, which is long enough to obtain a stable box size. Then, another NPT with a 1.0 fs time step and time was set to 1.0 ns, to record the trajectory for subsequent analysis. The atomic trajectories are every 1000 femtoseconds. where the temperature is set to 298.15 K.

In all the MD simulations, the motion of atoms was described by classical Newton's equations, which were solved using the velocity-Verlet algorithm. And all the Molecular Dynamics simulations were performed by using the GROMACS 2022.2 package [38]. The results were analyzed using the Gromacs tool suite, the Visual Molecular Dynamics program (VMD) [39], and additional scripts written by the researchers.

3. Results and Discussion

In polymer-based solid-state electrolytes, ion transport kinetics are governed by two critical structural parameters: the available free volume and the spacing between oxygen coordination sites along the polymer chains (Figure 1a). Free volume refers to the unoccupied space between molecular chains that enables the rearrangement and movement of ions—analogous to the interstitial voids in a densely packed assembly of spheres. For ion migration to occur, a contiguous free volume cavity with dimensions at least matching those of the migrating ion must be accessible. A larger free volume generally facilitates ion diffusion, as reflected in the relationship $D \propto \exp(-\gamma v^*/v_f)$ [40–42], where v^* is the critical minimum free volume required for ion hopping, v_f is the average free volume, and γ is the numerical factor to correct the overlap of the free volume.

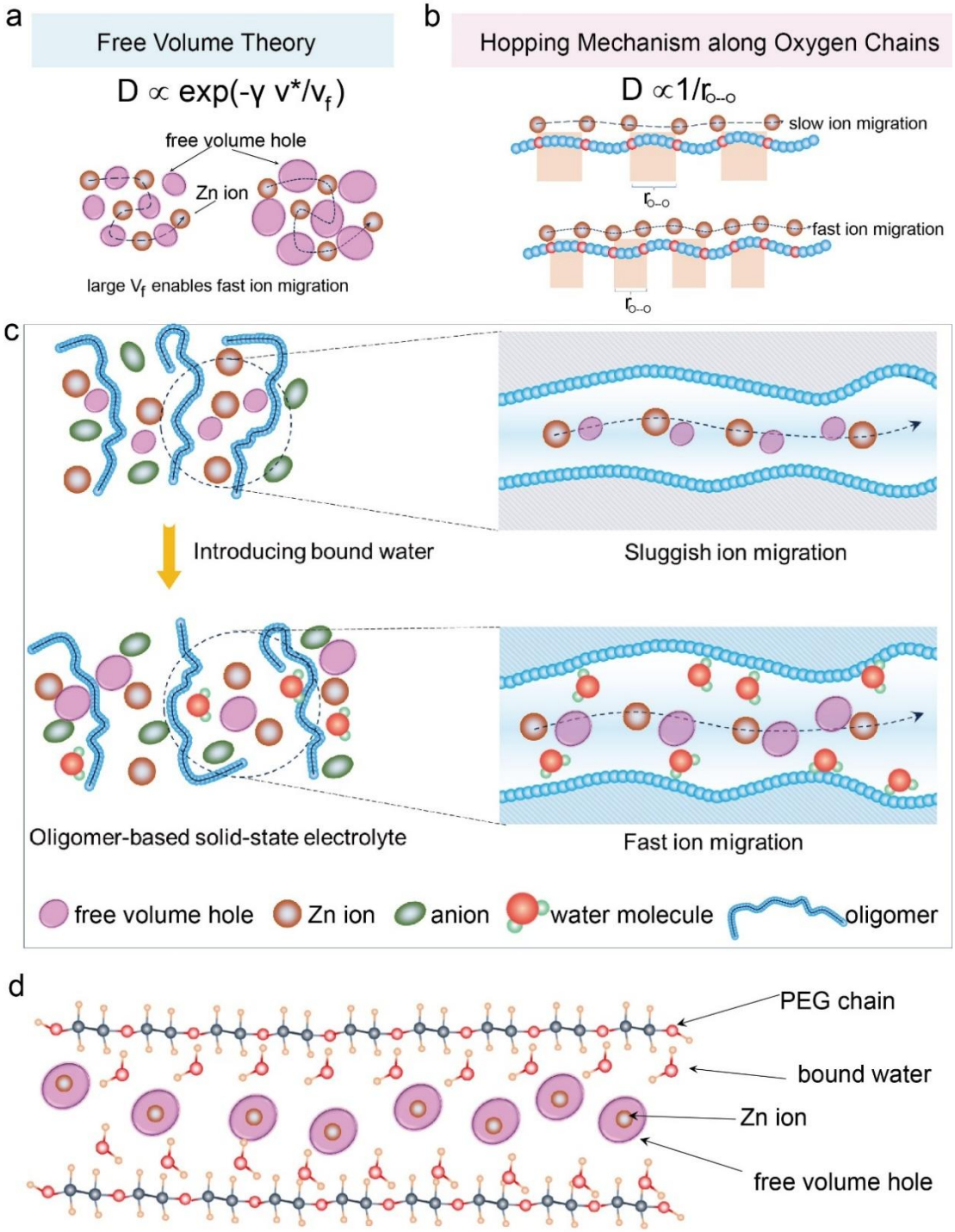

Figure 1. (**a**) Schematic illustration of the influence of free volume size on the migration of zinc ions. (**b**) Schematic depicting the effect of the distance between coordination sites on the mobility of zinc ions. (**c**) Illustration of the facilitating role of bound water in polymer-based solid electrolytes in enlarging free volume and shortening ion hopping distance. (**d**) Schematic representation of the interaction between bound water and PEG400 molecular chains in the solid electrolyte system studied in this work.

On the other hand, ion migration in such systems primarily follows a coordination-exchange mechanism, whereby ions hop sequentially between adjacent binding sites along the polymer chains (Figure 1b). The distance between these coordination sites thus represents another key parameter governing ion migration kinetics [43,44]. A shorter hopping distance generally corresponds to a lower energy barrier, thereby promoting faster ion transport. In conventional polymer-based solid electrolytes, however, strong interchain interactions often give rise to densely packed segments, which restrict free volume and lead to sluggish ion mobility (Figure 1c). The incorporation of bound water alleviates these limitations through a dual mechanism. First, water acts as a plasticizer, weakening polymer–polymer interactions, inducing chain swelling, reducing crystallinity, and consequently expanding the

free volume—collectively facilitating ion movement (Figure 1c). Second, water molecules form hydrogen bonds with oxygen atoms along the polymer backbone, effectively serving as bridging units that shorten the hopping distance between adjacent zinc-ion coordination sites. This synergistic effect significantly enhances long-range ion migration (Figure 1c,d), ultimately resulting in markedly improved macroscopic ionic mobility.

To systematically evaluate the influence of water content on ionic conductivity, we prepared a series of five viscoelastic solid-state electrolyte (V-SSE) systems with varying water contents. Rheologically, V-SSEs behave as viscoelastic solids, sharing similarities with everyday materials such as toothpaste, facial creams, plasticine, and dough. These systems retain their shape without flowing under static conditions, yet exhibit liquid-like deformability under slight external stress, along with excellent ductility and plasticity at room temperature. As a result, V-SSEs not only achieve an effective balance among ion transport, interfacial compatibility, and zinc anode electrochemical stability, but also offer straightforward processability under ambient conditions (room temperature and low pressure). Figure 2a provides a comprehensive schematic of the V-SSE structure and its key constituents. The viscous matrix consists of PEG400, a linear polymer with the structure HO-$(CH_2CH_2O)_n$-H, containing approximately nine repeating ethoxy units ($n \approx 9$), which is liquid at room temperature (Figure S1). As reported in our previous work [35], the incorporation of nano-silica filler induces a liquid-to-solid transition, yielding a self-standing viscoelastic electrolyte.

The selection of PEG400 as the polymer matrix was based on two primary considerations. First, the relatively low molecular weight of PEG400 allows it to function as an effective viscous matrix, facilitating the construction of a solid electrolyte with a viscoelastic structure. Second, PEG400 possesses a low degree of polymerization ($n \approx 9$), which enables a precise comparison of the molar ratio between water molecules and ether oxygen atoms in the repeating units. The nano-silica functions as an elastic scaffold, while zinc trifluoromethanesulfonate is employed as the zinc salt owing to its high degree of dissociation and favorable solubility in PEG400 without requiring additional solvents. The water content was carefully controlled below 20 wt% to prevent the formation of free liquid water, thereby distinguishing the system from conventional liquid aqueous or quasi-solid hydrogel electrolytes and preserving an entirely solid architecture. A series of V-SSE samples with water contents of 0%, 6.64%, 9.16%, 16.43%, and 19.87% (by mass) were prepared and designated accordingly. All obtained electrolytes displayed a plasticine-like solid morphology (Figure 2b), characterized by high homogeneity, semi-transparency, and outstanding plasticity, attributable to a dynamic weak-bond network. These materials could be easily rolled into thin films under low pressure (Figure 2c), and large-area membranes were successfully fabricated, enabling versatile battery assembly in formats such as coin-type and pouch cells.

Given the low water content in the samples, the formation of free water was effectively prevented. The state of water was further examined by T_2 relaxation time analysis using low-field nuclear magnetic resonance (LF-NMR). The T_2 relaxation time reflects the binding state and mobility of hydrogen protons, providing insight into their chemical environment. Generally, more tightly bound or less mobile hydrogen protons exhibit shorter T_2 relaxation times, resulting in a left-shifted peak in the T_2 spectrum. Based on this principle, the spin–spin relaxation time (T_2) of V-SSE samples with different water contents was measured to analyze the state of water molecules. Figure 2d shows the T_2 relaxation curves of the V-SSE samples. The horizontal axis (x-axis) represents the relaxation time (ms) of hydrogen protons, and the vertical axis (y-axis) indicates the relative quantity of hydrogen protons at each relaxation time. Typically, strongly bound and weakly bound water exhibit T_2 relaxation times in the range of 0.1 to 10 ms, while free water shows T_2 values between 100 and 1000 ms. The relaxation time of the anhydrous sample was 2.63 ms, corresponding to hydrogen protons in PEG400. As the water content increased, the T_2 values shifted toward longer relaxation times, reaching 3.18 ms, 3.55 ms, 5.93 ms, and 7.46 ms, respectively. No relaxation peak was observed above 100 ms (Table S1), confirming the absence of free water molecules and indicating that all water present was in a bound state. Despite the increase in water content, the electrochemical window does not narrow significantly and is maintained at approximately 2.82 V (Figure 2e), owing to the effective exclusion of free water. This demonstrates that the electrolyte's electrochemical stability is well preserved across the entire water content range studied (0–19.87%).

SEM characterization revealed uniform morphologies in both anhydrous and hydrated V-SSE systems (Figures 2f, S2, and S3). Energy-dispersive X-ray spectroscopy (EDS) confirmed the homogeneous distribution of all constituent elements (C, O, F, S, Si, Zn), reflecting the high compositional consistency of the composite (Figures 2g, S4, and S5). Furthermore, high-resolution time-of-flight secondary ion mass spectrometry (TOF-SIMS) analysis conducted in both positive and negative ion modes demonstrated that the spatial distributions of key species—including C, O, H, Si, F, S, and Zn—were highly consistent between the hydrated (Figures 2h, S6 and S7) and anhydrous systems (Figures 2i, S8 and S9). Together, these multi-technique characterizations verify the uniform elemental distribution within the V-SSE at the microscopic scale, confirming excellent sample homogeneity through complementary ion-detection modalities.

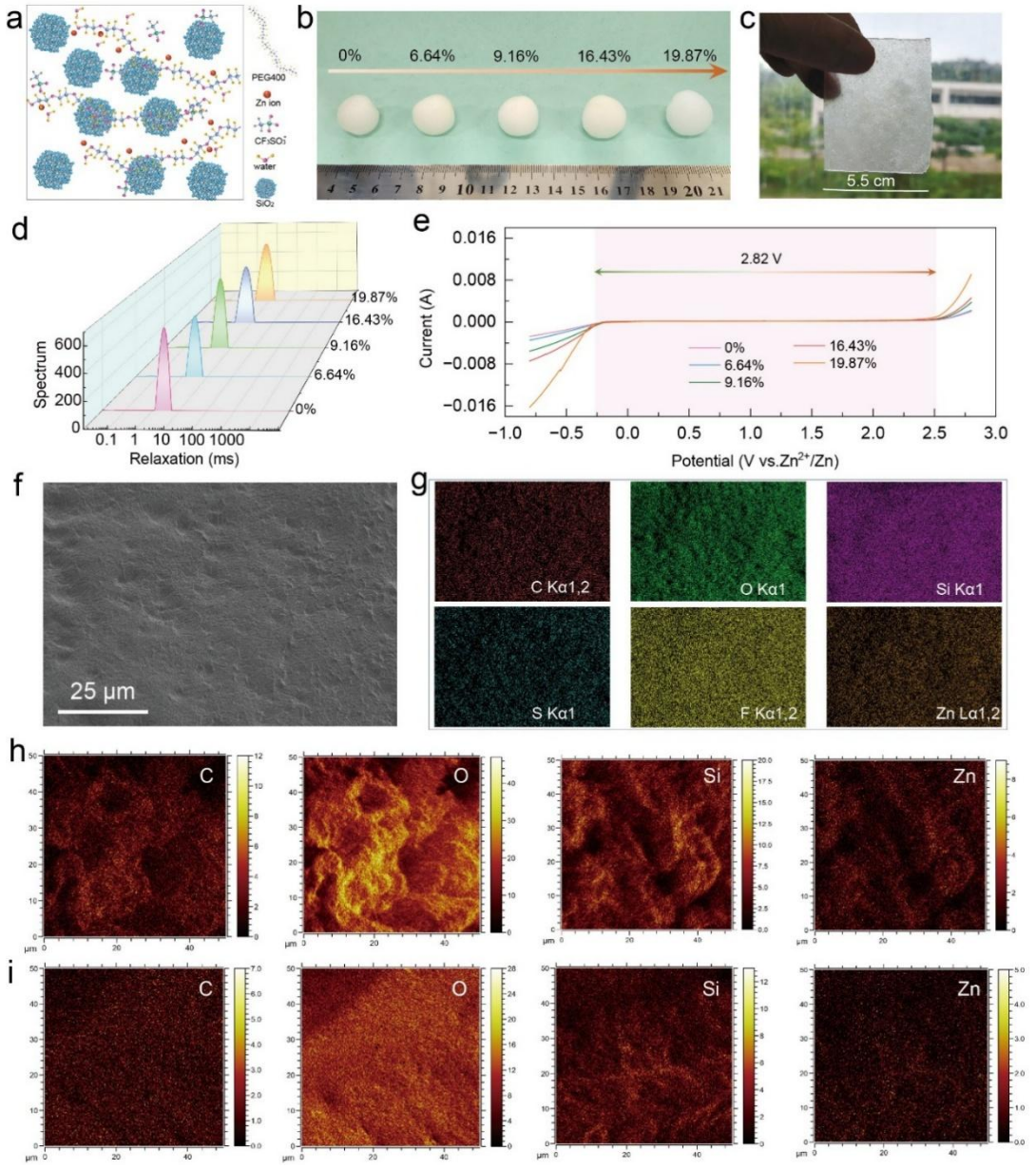

Figure 2. (**a**) Schematic illustration of the V-SSE composition. (**b**) Photographs of V-SSE with different water contents. (**c**) Images demonstrating the rolling process into a freestanding film, shown for V-SSE with 16.43% water content. (**d**) Low-field NMR spectra of V-SSE with varying water contents. (**e**) Linear sweep voltammetry (LSV) curves of C||Zn cells employing V-SSE with different water contents. (**f**) SEM image of V-SSE (0%) and (**g**) corresponding EDS elemental distribution map. Elemental mapping based on time-of-flight secondary ion mass spectrometry (TOF-SIMS): (**h**) V-SSE (19.87%) and (**i**) V-SSE (0%).

To evaluate the effect of water content on V-SSE performance, Zn||Zn symmetric cells were first assembled and analyzed. The ionic conductivity of the electrolyte governs the zinc deposition overpotential, which can be directly probed using such symmetric cells. The voltage polarization behavior of V-SSEs with different water contents was examined under various current densities and areal capacities. Figure 3a displays the voltage–time profiles of Zn||Zn cells incorporating V-SSEs with varying water contents, tested with stepwise increasing current densities from 0.2 to 1.0 mA cm^{-2} and areal capacities from 0.2 to 1.0 mAh cm^{-2}. At a low current density of 0.2 mA cm^{-2} and an areal capacity of 0.2 mAh cm^{-2}, all cells—across water contents ranging from 0% to 19.87%—exhibited stable zinc plating/stripping behavior. The voltage hysteresis was found to be only 0.22 V for the sample with 19.87% water content. In contrast, the voltage hysteresis progressively increased to 0.23, 0.32, 0.35, and 0.38 V for water contents of 16.43%, 9.16%, 6.64%, and 0%, respectively (Figure 3b), corresponding to a 4.54% to 72.7% increase relative to the 0.22 V benchmark. When the current density and areal capacity were increased to 0.5 mA cm^{-2} and 0.5 mAh cm^{-2}, the voltage hysteresis values became 0.40 V, 0.41 V, 0.61 V, 0.76 V, and 0.83 V, representing increases of 2.50%, 52.5%, 90.0%, and 107% relative to the 0.40 V, respectively.

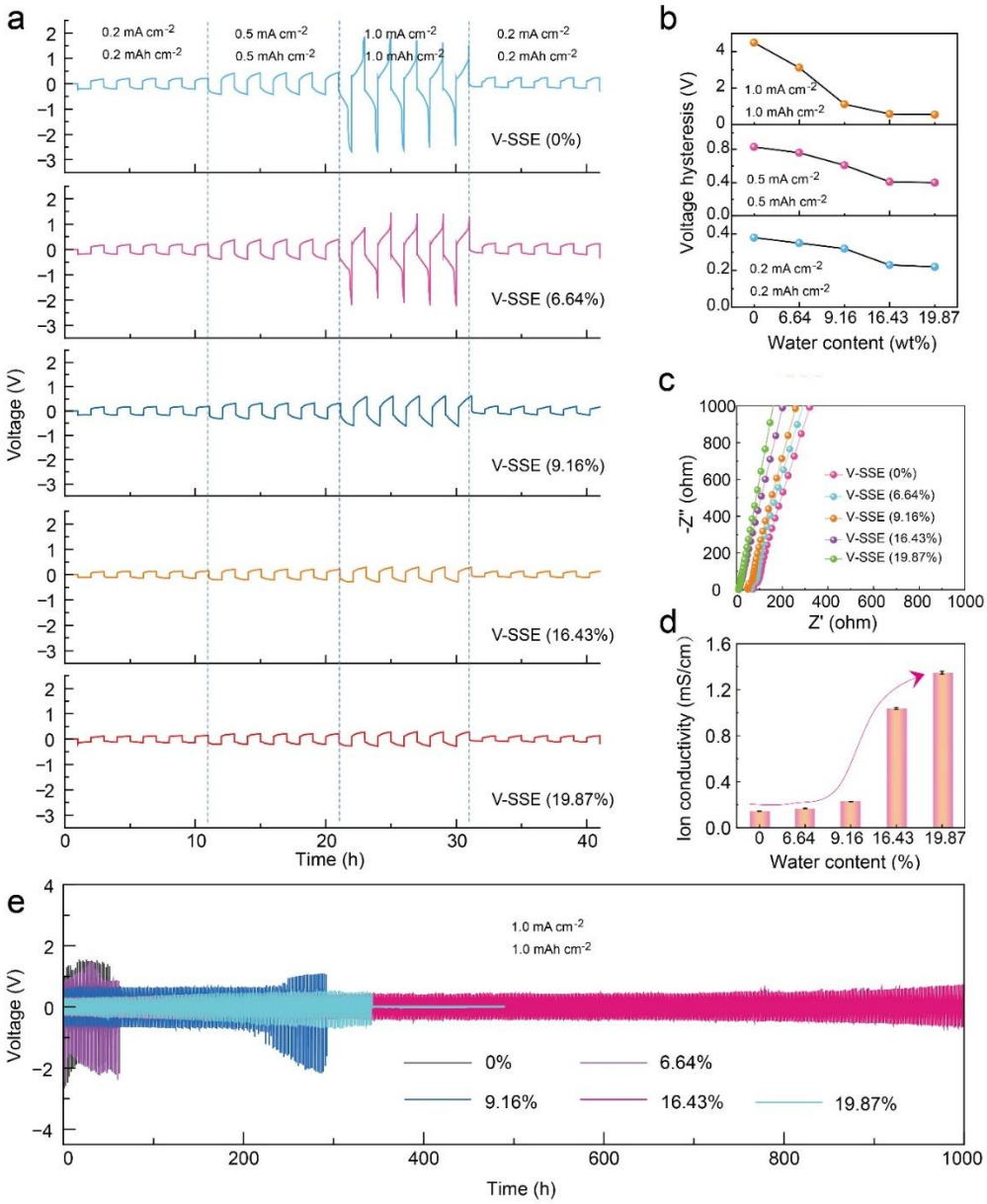

Figure 3. (**a**) Voltage–time profiles of Zn||Zn symmetric cells using V-SSE with different water contents, measured under various current densities and deposition capacities. (**b**) Corresponding voltage hysteresis as a function of water content. (**c**) Electrochemical impedance spectra of SS||SS symmetric cells employing V-SSE with different water contents. (**d**) Ionic conductivity of V-SSE versus water content. (**e**) Long-term voltage–time profiles of Zn||Zn symmetric cells with V-SSE under 1 mA cm^{-2} and 1 mAh cm^{-2} cycling conditions.

Further increasing the current density and areal capacity to 1.0 mA cm^{-2} and 1.0 mAh cm^{-2} resulted in voltage hysteresis values of 0.55 V, 0.58 V, 1.12 V, 3.12 V, and 4.49 V, with increases of 5.45%, 104%, 467%, and 716% relative to the 0.55 V. These results reveal that cells with water contents between 0% and 6.64% could only operate stably under low current densities (0.2–0.5 mA cm^{-2}) and low areal capacities (0.2–0.5 mAh cm^{-2}). Under high current/capacity conditions, severe polarization emerged, reflecting a substantial increase in interfacial kinetic resistance. In contrast, cells containing 16.43% to 19.87% water exhibited relatively small voltage hysteresis across both low and high current densities, indicating superior charge transfer kinetics. These findings underscore the crucial role of appropriate water content in facilitating efficient charge transport within the electrolyte.

The ionic conductivity results underscore the crucial role of water content in governing ion transport behavior. Symmetric SS||SS cells were fabricated using V-SSE with water contents ranging from 0% to 19.87%, and their impedance characteristics were evaluated by electrochemical impedance spectroscopy (EIS) (Figures 3c and S10–S14). All EIS measurements were conducted under controlled conditions: 25 °C, identical electrolyte area (1.95 cm^{-2}) and consistent thickness (approximately 200 μm), and the reported ionic conductivity values represent averages from three independent tests to ensure data reliability (Table S2). As depicted in Figure 3d, the ionic

conductivity evolves in distinct stages with increasing water content. At low water levels (0% and 6.64%), the conductivity remains highly constrained, varying only between 0.144 and 0.167 mS cm^{-1}. Beyond 6.64% water content, a progressive enhancement in ionic conductivity is observed.

The ionic conductivity rises marginally to 0.229 ± 0.002 mS cm^{-1} with a water content of 9.16%. A further increase to 16.43% water content, however, triggers a sharp surge in conductivity to 1.04 ± 0.008 mS cm^{-1}. This value, which is over seven times higher than that of the anhydrous electrolyte, signifies the formation of highly efficient ion transport pathways. Further increasing the water content to 19.87% results in only a modest improvement to 1.35 ± 0.012 mS/cm, suggesting the onset of a plateau region where additional water does not substantially improve ion transport. This trend in conductivity is fully consistent with the rate-dependent performance observed in Zn||Zn symmetric cells.

High ionic conductivity is essential for achieving stable cycling of solid-state cells under high current density and large areal capacity. As shown in Figure 3e, the long-term cycling performance of V-SSEs with different water contents was evaluated under demanding conditions of 1 mA cm^{-2} and 1 mAh cm^{-2}, corresponding to a zinc utilization of ~12% based on the 17 μm-thick Zn foil employed. It is evident that systems with high ionic conductivity (greater than 1 mS/cm) exhibit significantly extended cycle life, ranging from 340 to 1000 h. In contrast, systems with conductivity below 1 mS/cm suffer from shortened cycle lifetimes (less than 220 h) and pronounced voltage hysteresis (1.2–3.6 V) (Figures S15–S20). This behavior can be rationalized in terms of ion transport kinetics: high ionic conductivity reduces interfacial impedance, promotes uniform zinc deposition, suppresses dendrite formation, and thereby prolongs cell lifespan. It is noteworthy that although V-SSE with 19.87% water exhibits higher ionic conductivity than that with 16.43%, its cycling stability is compromised. This suggests the existence of an optimal water content threshold. While excessive water enhances ionic conductivity, it also induces detrimental side reactions: (1) Accumulation of interfacial by-products—water reacts with zinc metal to form insulating layers, leading to increased polarization in later cycling stages (Figure S21); and (2) Electrolyte decomposition—water participates in the breakdown of electrolyte components, accelerating capacity fade. Therefore, precise regulation of water content is essential to simultaneously achieve high ionic conductivity and long-term cycling stability.

Based on the preceding results, the ionic conductivity of the electrolyte is clearly enhanced once the water content exceeds a specific threshold. To clarify the role of water in ion conduction, we analyzed the system from the perspectives of free volume theory and the ion-hopping mechanism between coordination sites. For a more quantitative analysis, we calculated the molar ratio of water molecules to ether oxygen (EO) units in the repeating—CH_2CH_2O—segments of PEG400 within V-SSEs of different water contents, given that EO groups act as the primary coordination sites for Zn^{2+} migration. The resulting samples exhibited H_2O:EO molar ratios of 0, 1:3, 1:2, 1:1, and 1.5:1.

According to the free volume theory, the efficiency of ion transport is strongly correlated with the free volume available within the electrolyte matrix. To quantitatively assess the influence of water content on free volume in the V-SSE, positron annihilation lifetime spectroscopy (PALS) measurements were conducted. Typical PALS analysis revealed three lifetime components (Figure 4a, Table S3) [45–47]: τ_1 corresponds to the self-annihilation of para-positronium (p-Ps); τ_2 arises from the annihilation of free positrons and their interactions with molecular species; and τ_3 is associated with the pick-off annihilation of ortho-positronium (o-Ps) in molecular voids. Each lifetime component τ_i is accompanied by a corresponding intensity I_i (Table S3), representing the relative abundance of annihilation events with that specific lifetime. Importantly, the third component (τ_3, I_3) is directly related to free volume properties, as τ_3 reflects the local electron density at o-Ps annihilation sites, which correspond to intermolecular and intramolecular voids within the matrix. The annihilation lifetime parameters allow the calculation of the average free-volume cavity size and the fractional free volume (FFV) (Equations (4)–(6)), thereby providing quantitative insights into the nanostructural features of the electrolyte that are critical for ion transport.

$$\frac{\tau}{ns} \approx \frac{1}{2}\left(1 - \frac{R}{R+\Delta R} + \frac{1}{2\pi}\sin\frac{2\pi R}{R+\Delta R}\right)^{-1} \tag{4}$$

where τ denotes the o-Ps lifetime, ΔR is an empirical parameter (0.166 nm).

$$V_f = \frac{4}{3}\pi R^3 \tag{5}$$

where V_f is the free volume and R is the radius of the free volume hole as obtained by the o-Ps lifetime using Equation (4).

$$FFV = CV_f I_3 \tag{6}$$

where I_3 is the intensity of the o-Ps, and C is the empirically determined constant (0.0018 $Å^{-3}$).

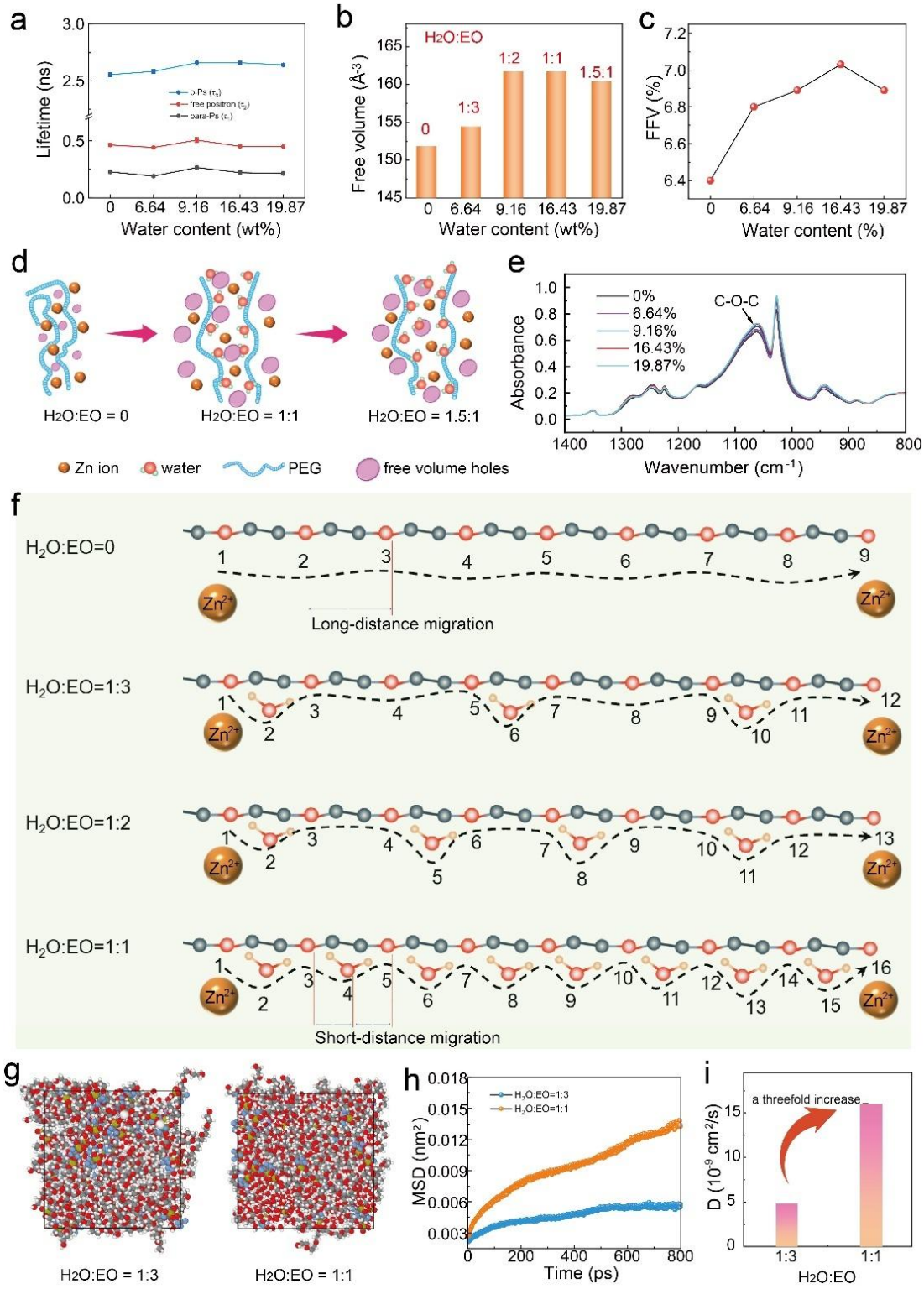

Figure 4. (**a**) The lifetime values of para-Ps (τ_1), free positron (τ_2) and o-Ps (τ_3) of V-SSE with different water content. Comparison of the (**b**) free volume and (**c**) FFV of V-SSE with different water content. (**d**) Schematic illustration of the influence of water content on free volume. (**e**) FTIR spectra of V-SSE with different water content. (**f**) Schematic illustration of rapid ion migration mediated by bound water through shortening the zinc-ion diffusion path. (**g**) A typical V-SSE structure consisting of different water content. (**h**) The mean square displacement (MSD) of Zn ion in V-SSE with different H_2O:EO ratios, and (**i**) the corresponding diffusion coefficient of Zn^{2+} ions.

The free volume was observed to increase gradually with water content, expanding from approximately 152 Å^3 in the anhydrous system to about 163 Å^3 (Figure 4b), indicating that water molecules effectively enlarge the pore structure of the V-SSE. The free volume reached a maximum at H_2O:EO ratios between 1:2 and 1:1. Beyond this range, further increases in water content led to a slight contraction in free volume, suggesting that excess water

molecules occupy and reduce the available space. A similar trend was observed for the fractional free volume (FFV) (Figure 4c). Notably, however, ionic conductivity increased monotonically with water content, implying that factors beyond free volume govern ion transport. Even at 19.87% water (H_2O:EO = 1.5:1), no free liquid water was detected, confirming that the high ionic conductivity does not stem from liquid-phase diffusion but rather from a structural ion-hopping mechanism. Although excess water slightly reduces free volume, it simultaneously increases the density of hopping sites and shortens the average ion-jump distance, thereby accelerating ion diffusion.

Upon introduction into the electrolyte system, water molecules initially reside in the existing free volume between polymer chains. However, as reported in previous studies, water incorporation can also induce polymer swelling and generate new free volume sites [48]. Specifically, water molecules promote chain expansion (Figure 4d), leading to a net increase in free volume. This swelling effect stems from the ability of water to form hydrogen bonds with polar groups along the polymer backbone, such as ether oxygen units (–C–O–C–). These bound water molecules intercalate between adjacent polymer chains, effectively screening strong dipole–dipole interactions between ether oxygen groups. As a result, chain entanglement and interchain cohesion are reduced. Moreover, water disrupts local ordering and enhances conformational disorder within the polymer matrix, further promoting free volume formation. The resulting increase in segmental mobility facilitates chain rearrangement and the formation of larger interchain voids, collectively expanding the free volume. This structural expansion contributes to enhanced ion transport and higher ionic conductivity. However, when water is introduced in excess, it begins to occupy pre-existing free volume cavities. At high concentrations, this occupancy reduces the overall free volume fraction, counteracting the initial swelling effect.

Based on the foregoing analysis, bound water influences ion transport through mechanisms beyond free volume modulation. It is well established that bound water can weaken the strong coordination between Zn^{2+} ions and ether oxygen groups, thereby lowering the dissociation energy barrier and increasing the concentration of mobile Zn^{2+} species. Figure 4e presents the Fourier-transform infrared (FTIR) spectra of V-SSEs with different water contents. The absorption band at 1062 cm^{-1} is assigned to ether oxygen groups complexed with Zn^{2+} ions [35]. As water content increases, this peak exhibits a slight increase in intensity and shifts to lower wavenumbers (Figure S22), indicating that water molecules disrupt the original strong Zn^{2+}–ether oxygen coordination, leading to a more labile and dynamic coordination environment involving water molecules. This suggests that water acts not merely as a plasticizer, but also participates directly in modulating the Zn^{2+} coordination structure. By competing for coordination sites, water effectively reduces the migration energy barrier for Zn^{2+}, consistent with the marked enhancement in ionic conductivity. The underlying mechanism involves the formation of hydrogen bonds between water molecules and ether oxygen groups (O–H···O), which reduces the C–O bond vibration frequency. The associated hydrogen bonding can also induce spectral peak broadening, as is subtly observed in our FTIR spectra (Figure 4e) [49,50].

It is noteworthy that the ether oxygen vibrational bands nearly coincide in the V-SSE (16.43%) and V-SSE (19.87%) systems, indicating that the modulating effect of water content on Zn–O coordination weakening has reached saturation. Nevertheless, conductivity measurements reveal a further significant increase in ionic conductivity for V-SSE (19.87%). Raman spectroscopy also revealed minimal spectral shifts (Figures S23 and S24). The band observed near 1114 cm^{-1} is attributed to the asymmetric stretching vibration of the C–O–C group coordinated with Zn^{2+}. Coordination between Zn^{2+} and the ether oxygen atom reduces the electron density of the C–O–C bond, increasing the vibrational energy and resulting in a blue shift of the corresponding peak. As the water content increased from 0% to 19.87%, the position of this peak showed only a slight shift, moving from 1113.0 cm^{-1} to 1113.1 cm^{-1}, 1115.0 cm^{-1}, 1115.4 cm^{-1}, and finally 1116.2 cm^{-1}. These results imply that additional mechanisms facilitate zinc ion transport at higher water content. Fast ion transport is often associated with hopping between oxygen coordination sites [51–53], where the distance between adjacent sites is a critical factor. Water molecules may shorten the ion hopping distance between neighboring ether oxygen sites through hydrogen bonding (Figure 4f), providing a plausible explanation for the notable conductivity improvement at H_2O:EO = 1:1, as well as the further enhancement in conductivity with additional water—even when free volume is reduced.

Molecular dynamics simulations (Figures 4g, S25, and S26) reveal a marked enhancement in the mean square displacement (MSD) of Zn^{2+} ions under the H_2O:EO = 1:1 condition compared to the H_2O:EO = 1:3 case. Over a simulation period of 800 ps, the MSD of Zn^{2+} ions at H_2O:EO = 1:1 reaches 0.014 nm^2, a value three times greater than that observed at H_2O:EO = 1:3 (0.0055 nm^2) (Figure 4h). Correspondingly, the Zn^{2+} diffusion coefficient under H_2O:EO = 1:1 attains 16×10^{-9} cm^2/s, representing a threefold increase over the value measured at H_2O:EO = 1:3 (Figure 4i). These results indicate substantially faster and more extensive mobility of Zn^{2+} ions in the H_2O:EO = 1:1 electrolyte environment. This enhanced ion transport is primarily attributed to a significant shortening of the ion-

hopping distance and the formation of continuous, long-range conduction pathways, consistent with the exponential decay of hopping rate with increasing separation between coordination/solvation sites [54].

This water-mediated zinc-ion migration mechanism offers a promising strategy for designing high-performance solid-state zinc-ion batteries. To validate this concept, we assembled Zn||I_2 batteries employing water-mediated V-SSE and evaluated their electrochemical performance over a wide voltage range. Specifically, the anhydrous V-SSE (0%) was compared with two high-conductivity systems: V-SSE (19.87%) and V-SSE (16.43%). A schematic of the Zn||I_2 battery configuration is shown in Figure 5a, with an areal iodine loading of 1–2 mg cm^{-2} in the cathode. Figure 5b,c displays the charge–discharge profiles of batteries using anhydrous and hydrated V-SSE (19.87%) during the 1st and 10th cycles (Figure 5b,c), respectively. The anhydrous system delivered a limited specific capacity of only 94 mAh g^{-1} (Figure 5b), whereas the hydrated (19.87%) V-SSE significantly increased the discharge capacity to 208 mAh g^{-1}—more than double that of the dry electrolyte—along with a high initial Coulombic efficiency of 97%. This enhancement is attributed to the superior ionic conductivity of the hydrated electrolyte, which facilitates more complete utilization of the iodine cathode and improves interfacial kinetics with the zinc anode.

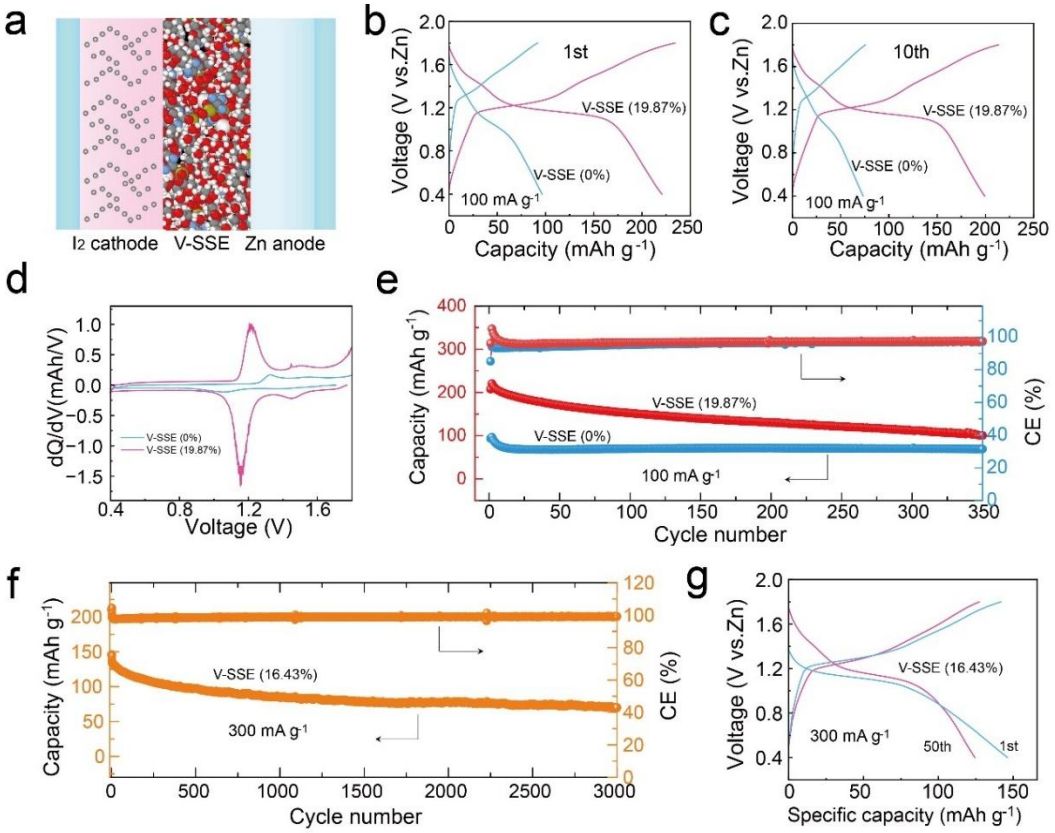

Figure 5. (**a**) Schematic illustration of the Zn|V-SSE|I_2 battery configuration. Charge–discharge profiles of Zn||I_2 batteries with V-SSE (0%) and V-SSE (19.87%) at a current density of 100 mA g^{-1} during the first (**b**) and tenth cycle (**c**). (**d**) Differential capacity (dQ/dV) curves of Zn||I_2 full cells using V-SSE (0%) versus V-SSE (19.87%) at 100 mA g^{-1}. (**e**) Long-term cycling performance of Zn||I_2 full cells with V-SSE (0%) and V-SSE (19.87%) at 100 mA g^{-1}. (**f**) Long-cycle performance of Zn||I_2 full cells with V-SSE (16.43%) at 300 mA g^{-1}, and (g) corresponding charge–discharge profiles.

Differential capacity (dQ/dV) curves further revealed that the redox peak intensities were markedly stronger in the hydrated system than in the anhydrous counterpart (Figure 5d), indicating superior ion diffusion kinetics at the electrolyte/electrode interface. Long-term cycling performance demonstrated that the hydrated V-SSE (19.87%) also maintained good stability, retaining 50% of its capacity after 350 cycles (Figure 5e). Both the V-SSE (0%) and V-SSE (19.87%) systems exhibited rapid capacity decay during the initial 10 cycles, which can be attributed to interfacial side reactions caused by the instability of terminal hydroxyl groups in PEG400 [55,56]. For the V-SSE (0%) system, almost no capacity fade was observed between cycles 10 and 350. This excellent cycling stability is ascribed to its relatively low initial capacity and the absence of water-induced parasitic reactions. In contrast, the V-SSE (19.87%) system showed gradual capacity decay over the same cycling interval (cycles 10–350), which arises from the following two factors. First, the relatively high iodine loading in the cathode material

(iodine accounts for more than 50% of the iodine/activated carbon composite cathode) may lead to partial iodine sublimation from the carbon host, resulting in active mass loss and capacity decline. Second, the presence of bound water could also induce interfacial side reactions during long-term cycling. Therefore, rational regulation of bound water content is essential to achieve more stable electrochemical performance. The use of V-SSE with 16.43% water content led to further extension of the cycle life. As shown in Figure S27, the cell maintained stable cycling for over 700 cycles at 100 mA g^{-1}, retaining a capacity of 170 mAh g^{-1}. Even under a higher current density of 300 mA g^{-1}, the cell exhibited enhanced stability over 3000 cycles (Figure 5f) with highly reversible charge/discharge behavior (Figure 5g). These results demonstrate that through rational modulation of water content, excellent long-term cycling performance can be achieved while maintaining rapid ion conduction.

It should be noted that V-SSE, as a solid electrolyte with a unique condensed-state structure, offers potential multi-dimensional advantages in energy storage batteries and effectively addresses key limitations of conventional solid-state electrolytes. In terms of electrochemical performance, it not only exhibits high ionic conductivity at room temperature, benefiting from its intrinsic dynamic weak interaction, but also possesses liquid-like interfacial compatibility. The advantages in fabrication and processability are even more pronounced: the entire preparation process is environmentally benign, requiring no volatile or highly toxic organic solvents, which eliminates liquid waste generation from the source and reduces environmental treatment costs (Figure 6). Moreover, the synthesis procedure is straightforward, enabling scalable production without the need for complex equipment, thus laying a foundation for industrial adoption. The resulting V-SSE material also exhibits excellent processing compatibility, allowing it to be directly fabricated into uniform and dense thin films under mild conditions (room temperature and low pressure). These thin films can be applied onto paper (e.g., filter paper) or fabric (e.g., filter cloth), or as self-standing films, then integrated into battery assemblies without additional treatments, significantly streamlining the manufacturing process and reducing production costs.

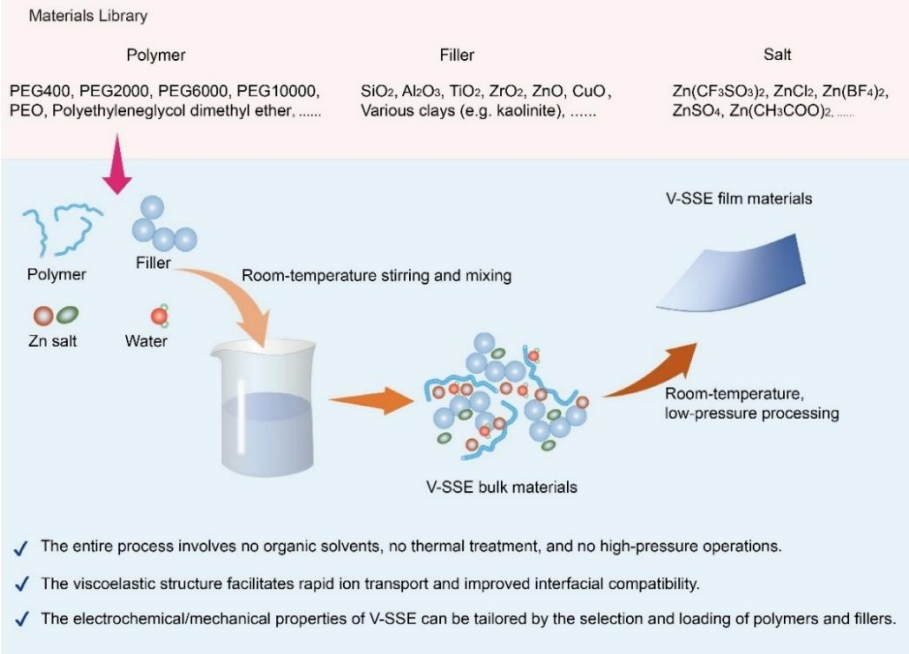

Figure 6. Schematic of V-SSE's superiority in scalable fabrication and performance tunability.

Notably, the properties of V-SSE are highly tunable. By strategically selecting polymer matrices, inorganic fillers, and zinc salts (as exemplified in zinc-ion battery systems) from commercially available material libraries and by precisely adjusting their composition ratios, key characteristics such as ionic conductivity, interfacial stability, and mechanical strength can be directionally optimized to meet the requirements of different battery systems and application scenarios. When compared with other recently reported polymer or inorganic solid electrolytes [28,29,57–60], V-SSE demonstrates outstanding overall advantages in electrochemical performance, processability, and cost-effectiveness (Table S4). These benefits originate from its extremely simplified preparation pathway. While most conventional electrolyte syntheses rely on energy-intensive and complex steps—such as high-temperature sintering, extensive use of organic solvents, or high-pressure film formation, often accompanied by significant waste generation—V-SSE entirely circumvents these issues through a simple one-step mixing process. This approach not only ensures competitive performance but also substantially lowers production complexity and cost.

4. Conclusions

In this work, we systematically investigate the influence of bound water content on the ion conduction behavior of a V-SSE and elucidate the underlying mechanisms by which bound water enhances Zn^{2+} transport. We demonstrate that introducing a moderate amount of water significantly improves zinc-ion conductivity without substantially narrowing the electrochemical stability window. Notably, once the water content exceeds a threshold, the ionic conductivity increases markedly from ~10^{-4} S/cm to ~10^{-3} S/cm, indicating a substantial enhancement in ion mobility. The molar ratio of water to ether oxygen (EO) in the repeating units of poly(ethylene glycol) was identified as a critical descriptor. A distinct transition occurs at an H_2O:EO ratio of 1:1, accompanied by a pronounced jump in conductivity. Through systematic analysis of free volume and ion diffusion kinetics, we reveal that an appropriate water content expands the free volume, while excess water leads to a slight contraction. Nevertheless, the monotonic rise in ionic conductivity with water content implies that ion transport is not solely governed by free volume. The reduction in long-range ion-hopping distance also plays a critical role. We propose that water molecules serve as dynamic bridges between adjacent ether oxygen sites, significantly shortening the ion-hopping distance and reducing the migration energy barrier, thereby accounting for the abrupt conductivity surge at the critical H_2O:EO = 1:1 ratio. Zn||I_2 full cells incorporating the hydrated V-SSE exhibit a remarkable improvement in discharge capacity, increasing from 94 mAh g^{-1} (anhydrous V-SSE) to above 170 mAh g^{-1} (hydrated V-SSE). Moreover, optimizing the water content significantly extends the cycling stability. This study reveals the multifunctional role of bound water in boosting ionic conductivity and offers valuable design principles for next-generation high-performance solid-state batteries, including zinc-based and other metal-ion systems.

Supplementary Materials

The additional data and information can be downloaded at: https://media.sciltp.com/articles/others/2511031002269406/eChem-25090049-SUPPL.pdf. Figure S1: The molecular structure of PEG400, Figure S2: SEM images of V-SSE (0%), Figure S3: SEM images of V-SSE (19.87%), Figure S4: EDS mapping of V-SSE (0%), Figure S5: EDS mapping of V-SSE (19.87%), Figure S6: Elemental mapping of V-SSE (19.87%) based on time-of-flight secondary ion mass spectrometry (TOF-SIMS) using negative ion modes, Figure S7: Elemental mapping of V-SSE (19.87%) based on time-of-flight secondary ion mass spectrometry (TOF-SIMS) using positive ion modes, Figure S8: Elemental mapping of V-SSE (0%) based on time-of-flight secondary ion mass spectrometry (TOF-SIMS) using negative ion modes, Figure S9: Elemental mapping of V-SSE (0%) based on time-of-flight secondary ion mass spectrometry (TOF-SIMS) using positive ion modes, Figure S10: Electrochemical impedance spectra of SS|V-SSE|SS cells using V-SSE (0%), Figure S11: Electrochemical impedance spectra of SS|V-SSE|SS cells using V-SSE (6.64%), Figure S12: Electrochemical impedance spectra of SS|V-SSE|SS cells using V-SSE (9.16%), Figure S13: Electrochemical impedance spectra of SS|V-SSE|SS cells using V-SSE (16.43%), Figure S14: Electrochemical impedance spectra of SS|V-SSE|SS cells using V-SSE (19.87%), Figure S15: Voltage–time profiles of Zn||Zn symmetric cells with V-SSE under 1 mA cm^{-2} and 1 mAh cm^{-2} cycling conditions, Figure S16: Voltage–time profiles of Zn||Zn symmetric cells with V-SSE (0%) under 1 mA cm^{-2} and 1 mAh cm^{-2} cycling conditions, Figure S17: Voltage–time profiles of Zn||Zn symmetric cells with V-SSE (6.64%) under 1 mA cm^{-2} and 1 mAh cm^{-2} cycling conditions, Figure S18: Voltage–time profiles of Zn||Zn symmetric cells with V-SSE (9.16%) under 1 mA cm^{-2} and 1 mAh cm^{-2} cycling conditions, Figure S19: Voltage–time profiles of Zn||Zn symmetric cells with V-SSE (16.43%) under 1 mA cm^{-2} and 1 mAh cm^{-2} cycling conditions, Figure S20: Voltage–time profiles of Zn||Zn symmetric cells with V-SSE (19.87%) under 1 mA cm^{-2} and 1 mAh cm^{-2} cycling conditions, Figure S21: Voltage–time profiles of Zn||Zn symmetric cells during late cycle with V-SSE (16.43% vs. 19.87%) under 1 mA cm^{-2} and 1 mAh cm^{-2} cycling conditions, Figure S22: FTIR of V-SSE with different water content, Figure S23: Raman spectra of V-SSE with different water content, Figure S24: Raman spectra of V-SSE with different water content, Figure S25: A typical V-SSE structure with H_2O:EO = 1:3, Figure S26: A typical V-SSE structure with H_2O:EO = 1:1, Figure S27: Long-cycle performance of Zn||I_2 full cells with V-SSE (16.43%) at 100 mA g^{-1}, Table S1: T2 relaxation time of V-SSE samples, Table S2: Ionic conductivity of V-SSE versus water content, Table S3: Positron annihilation lifetime spectrum test results, Table S4: Comparison on the performance of the proposed V-SSE against other recently reported solid-state zinc-ion electrolytes.

Author Contributions

Y.C.: data curation, writing—original draft preparation, visualization, software; W.L.: formal analysis, project administration; L.X.: formal analysis, project administration; M.Y.: formal analysis, resources; Y.Z.: formal analysis, resources; Y.T.: formal analysis, resources; X.L.: formal analysis, resources; Z.W.: formal

analysis, resources; Q.(A.)Y.: formal analysis, resources; W.D.: conceptualization, methodology, supervision, project administration, writing-review & editing; C.L.: supervision, project administration, methodology, writing—review & editing, resources.

Funding

This work was financially supported by the National Natural Science Foundation of China (Grant No. 22275039, Grant No. 52271204, Grant No. U24A20569), and the Guangdong Provincial Key Laboratory of Plant Resources Biorefinery (2021B1212010011).

Data Availability Statement

The data that support the findings of this study are available from the corresponding author upon reasonable request.

Conflicts of Interest

The authors declare no conflict of interest.

Use of AI and AI-Assisted Technologies

No AI tools were utilized for this paper.

References

1. Guo, W.; Tian, Y.; Jiang, L. Asymmetric Ion Transport through Ion-Channel-Mimetic Solid-State Nanopores. *Acc. Chem. Res.* **2013**, *46*, 2834.
2. Farrington, G.C.; Briant, J.L. Fast Ionic Transport in Solids: Crystalline Solids with Liquid-like Ionic Conductivities Are Revolutionizing Solid-State Electrochemistry. *Science* **1979**, *204*, 1371.
3. Ohno, S.; Banik, A.; Dewald, G.F.; et al. Materials Design of Ionic Conductors for Solid State Batteries. *Prog. Energy* **2020**, *2*, 022001.
4. Angell, C. Recent Developments in Fast Ion Transport in Glassy and Amorphous Materials. *Solid State Ion.* **1986**, *18–19*, 72.
5. Chen, R.; Li, Q.; Yu, X.; et al. Approaching Practically Accessible Solid-State Batteries: Stability Issues Related to Solid Electrolytes and Interfaces. *Chem. Rev.* **2020**, *120*, 6820.
6. Thomas, F.; Mahdi, L.; Lemaire, J.; et al. Technological Advances and Market Developments of Solid-State Batteries: A Review. *Materials* **2024**, *17*, 239.
7. Wang, C.; Sun, X. The Promise of Solid-State Batteries for Safe and Reliable Energy Storage. *Engineering* **2023**, *21*, 32.
8. Yang, F.; Santos, E.C.D.; Jia, X.; et al. A Dynamic Database of Solid-State Electrolyte (DDSE) Picturing All-Solid-state Batteries. *Nano Mater. Sci.* **2024**, *6*, 256.
9. Chen, P.; Ding, B.; Dou, H.; et al. Ceramic–Polymer Composite Solid-State Electrolytes for Solid-State Lithium Metal Batteries: Mechanism, Strategy, and Prospect. *Small* **2025**, 2503743.
10. Yu, T.; Liu, Y.; Li, H.; et al. Ductile Inorganic Solid Electrolytes for All-Solid-State Lithium Batteries. *Chem. Rev.* **2025**, *125*, 3595.
11. Fan, L.-Z.; He, H.; Nan, C.-W. Tailoring Inorganic–Polymer Composites for the Mass Production of Solid-State Batteries. *Nat. Rev. Mater.* **2021**, *6*, 1003.
12. Wu, J.; Chen, W.; Hao, B.; et al. Garnet-Type Solid-State Electrolytes: Crystal-Phase Regulation and Interface Modification for Enhanced Lithium Metal Batteries. *Small* **2025**, *21*, 2407983.
13. Zhao, Z.; Wang, J.; Lv, Z.; et al. In-situ Formed All-amorphous Poly (ethylene oxide)-based Electrolytes Enabling Solid-State Zn Electrochemistry. *Chem. Eng. J.* **2021**, *417*, 128096.
14. Dai, T.; Wu, S.; Lu, Y.; et al. Inorganic Glass Electrolytes with Polymer-like Viscoelasticity. *Nat. Energy* **2023**, *8*, 1221.
15. Jian, S.; Cao, Y.; Feng, W.; et al. Recent Progress in Solid Polymer Electrolytes with Various Dimensional Fillers: A Review. *Mater. Today Sustain.* **2022**, *20*, 100224.
16. Xue, S.; Chen, S.; Fu, Y.; et al. Revealing the Role of Active Fillers in Li-ion Conduction of Composite Solid Electrolytes. *Small* **2023**, *19*, 2305326.
17. Liu, J.; Wang, T.; Yu, J.; et al. Review of the Developments and Difficulties in Inorganic Solid-State Electrolytes. *Materials* **2023**, *16*, 2510.
18. Xiao, Y.; Wang, Y.; Bo, S.-H.; et al. Understanding Interface Stability in Solid-State Batteries. *Nat. Rev. Mater.* **2019**, *5*, 105.

19. Zhang, S.; Long, T.; Zhang, H.; et al. Electrolytes for Multivalent Metal-Ion Batteries: Current Status and Future Prospect. *ChemSusChem* **2022**, *15*, e202200999.
20. Raza, S.; Bashir, T.; Hayat, A.; et al. Recent Progress and Fundamentals of Solid-State Electrolytes for All Solid-State Rechargeable Batteries: Mechanisms, Challenges, and Applications. *J. Energy Storage* **2024**, *92*, 112110.
21. O'Donnell, L.F.; Greenbaum, S.G. Review of Multivalent Metal Ion Transport in Inorganic and Solid Polymer Electrolytes. *Batteries* **2020**, *7*, 3.
22. Li, R.; Deng, R.; Wang, Z.; et al. The Challenges and Perspectives of Developing Solid-State Electrolytes for Rechargeable Multivalent Battery. *J. Solid State Electrochem.* **2023**, *27*, 1291.
23. Jeschull, F.; Hub, C.; Kolesnikov, T.I.; et al. Multivalent Cation Transport in Polymer Electrolytes—Reflections on an Old Problem. *Adv. Energy Mater.* **2024**, *14*, 2302745.
24. Tian, W.; Lin, G.; Yuan, S.; et al. Competitive Coordination and Dual Interphase Regulation of MOF-Modified Solid-State Polymer Electrolytes for High-Performance Sodium Metal Batteries. *Angew. Chem. Int. Ed.* **2025**, 64, e202423075.
25. Jones, S.D.; Bamford, J.; Fredrickson, G.H.; et al. Decoupling Ion Transport and Matrix Dynamics to Make High Performance Solid Polymer Electrolytes. *ACS Polym. Au* **2022**, *2*, 430.
26. Shinde, S.S.; Wagh, N.K.; Kim, S.; et al. Li, Na, K, Mg, Zn, Al, and Ca Anode Interface Chemistries Developed by Solid-State Electrolytes. *Adv. Sci.* **2023**, *10*, 2304235.
27. McAlpine, J.; Bloemendal, A.; Dahl, J.E.; et al. Modulating Entropic Driving Forces to Promote High Lithium Mobility in Solid Organic Electrolytes. *Chem. Mater.* **2023**, *35*, 3545.
28. Hou, Y.; Wei, Z.; Wu, Z.; et al. Regulating Dielectricity of A Polymer Electrolyte to Promote Cation Mobility for High-Performance Solid Zinc Hybrid Batteries. *Energy Environ. Sci.* **2024**, *17*, 3917.
29. Wang, J.; Zhao, Z.; Lu, G.; et al. Room-temperature Fast Zinc-Ion Conduction in Molecule-Flexible Solids. *Mater. Today Energy* **2021**, *20*, 100630.
30. Miao, C.; Wang, X.; Guan, D.; et al. Spatially Confined Engineering Toward Deep Eutectic Electrolyte in Metal-Organic Framework Enabling Solid-State Zinc-Ion Batteries. *Angew. Chem. Int. Ed.* **2024**, *63*, e202410208.
31. Yan, S.; Lu, Y.; Liu, F.; et al. Zwitterionic Matrix with Highly Delocalized Anionic Structure as an Efficient Lithium Ion Conductor. *CCS Chem.* **2023**, *5*, 1612.
32. Vélez, J.F.; Aparicio, M.; Mosa, J. Effect of Lithium Salt in Nanostructured Silica–Polyethylene Glycol Solid Electrolytes for Li-Ion Battery Applications. *J. Phys. Chem. C* **2016**, *120*, 22852.
33. Di Noto, V.; Longo, D.; Münchow, V. Ion-Oligomer Interactions in Poly(ethylene glycol)400/(LiCl)x Electrolyte Complexes. *J. Phys. Chem. B* **1999**, *103*, 2636.
34. Aurbach, D.; Lu, Z.; Schechter, A.; et al. Prototype Systems for Rechargeable Magnesium Batteries. *Nature* **2000**, *407*, 724.
35. Lin, W.; Zhou, K.; Xing, L.; et al. Viscoelastic Soft Solid Electrolytes Enable Fast Zinc Ion Conductance and Highly Stable Zinc Metal Anode. *Adv. Energy Mater.* **2025**, *15*, 2404545.
36. Martínez, L.; Andrade, R.; Birgin, E.G.; et al. PACKMOL: A Package for Building Initial Configurations for Molecular Dynamics Simulations. *J. Comput. Chem.* **2009**, *30*, 2157.
37. Kaminski, G.A.; Friesner, R.A.; Tirado-Rives, J.; et al. Evaluation and Reparametrization of the OPLS-AA Force Field for Proteins via Comparison with Accurate Quantum Chemical Calculations on Peptides. *J. Phys. Chem. B* **2001**, **105**, 6474.
38. Abraham, M.J.; Murtola, T.; Schulz, R.; et al. GROMACS: High Performance Molecular Simulations Through Multi-Level Parallelism from Laptops to Supercomputers. *SoftwareX* **2015**, *1–2*, 19.
39. Humphrey, W.; Dalke, A.; Schulten, K. VMD: Visual Molecular Dynamics. *J. Mol. Graph.* **1996**, *14*, 33.
40. Pas, S.J.; Ingram, M.D.; Funke, K.; et al. Free Volume and Conductivity in Polymer Electrolytes. *Electrochimica Acta* **2005**, *50*, 3955.
41. Miyamoto, T.; Shibayama, K. Free-Volume Model for Ionic Conductivity in Polymers. *J. Appl. Phys.* **1973**, *44*, 5372.
42. Bamford, D.; Dlubek, G.; Reiche, A.; et al. The Local Free Volume, Glass Transition, and Ionic Conductivity in A Polymer Electrolyte: A Positron Lifetime Study. *J. Chem. Phys.* **2001**, *115*, 7260.
43. Halat, D.M.; Snyder, R.L.; Sundararaman, S.; Choo, Y.; et al. Modifying Li^+ and Anion Diffusivities in Polyacetal Electrolytes: A Pulsed-Field-Gradient NMR Study of Ion Self-Diffusion$^+$. *Chem. Mater.* **2021**, *33*, 4915.
44. Kost, B.; Basko, M.; Kaźmierski, S.; et al. Polyacetals of Higher Cyclic Formals: Synthesis, Properties and Application as Polymer Electrolytes. *Polym. Chem.* **2025**, *16*, 598.
45. Ramya, P.; Ranganathaiah, C.; Williams, J.F. Experimental Determination of Interface Widths in Binary Polymer Blends from Free Volume Measurements. *Polymer* **2012**, *53*, 4539.
46. Mor, J.; Pandey, K.L.; Sharma, S.K. Correlation Between Free Volume Structure and Ionic Conductivity of A Poly(ethylene oxide) and Dendritic Fibrous Nanosilica Composite-based Electrolyte: An Investigation Using Positron Annihilation and Broadband Dielectric Spectroscopy. *Phys. Chem. Chem. Phys*. **2025**, 27, 10082.

47. Utpalla, P.; Sharma, S.K.; Sudarshan, K.; et al. Free Volume Correlation with AC Conductivity and Thermo-Mechanical Properties of Poly (ethylene oxide)-silica Nanocomposites. *Eur. Polym. J.* **2019**, *117*, 10.
48. Zhan, Y.; Fu, W.; Xing, Y.; et al. Advances in Versatile Anti-Swelling Polymer Hydrogels. *Mater. Sci. Eng. C* **2021**, *127*, 112208.
49. Brogly, M.; Bistac, S.; Bindel, D. Adsorption and Structuration of PEG Thin Films: Influence of the Substrate Chemistry. *Polymers* **2024**, *16*, 1244.
50. Rocco, A.M.; Moreira, D.P.; Pereira, R.P. Specific Interactions in Blends of Poly(ethylene oxide) and Poly(bisphenol A-co-epichlorohydrin): FTIR and Thermal Study. *Eur. Polym. J.* **2003**, *39*, 1925.
51. Brooks, D.J.; Merinov, B.V.; Goddard, W.A.; et al. Atomistic Description of Ionic Diffusion in PEO–LiTFSI: Effect of Temperature, Molecular Weight, and Ionic Concentration. *Macromolecules* **2018**, *51*, 8987.
52. Gao, Y.; Nolan, A.M.; Du, P.; et al. Classical and Emerging Characterization Techniques for Investigation of Ion Transport Mechanisms in Crystalline Fast Ionic Conductors. *Chem. Rev.* **2020**, *120*, 5954.
53. He, X.; Zhu, Y.; Mo, Y. Origin of Fast Ion Diffusion in Super-Ionic Conductors. *Nat. Commun.* **2017**, *8*, 15893.
54. Sharon, D.; Deng, C.; Bennington, P.; et al. Critical Percolation Threshold for Solvation-Site Connectivity in Polymer Electrolyte Mixtures. *Macromolecules* **2022**, *55*, 7212.
55. Yang, X.; Jiang, M.; Gao, X.; et al. Determining the Limiting Factor of the Electrochemical Stability Window for PEO-based Solid Polymer Electrolytes: Main Chain or Terminal –OH Group? *Energy Environ. Sci.* **2020**, *13*, 1318.
56. Rong, Z.; Sun, Y.; Yang, M.; et al. How the PEG Terminals Affect the Electrochemical Properties of Polymer Electrolytes in Lithium Metal Batteries. *Energy Storage Mater.* **2023**, *63*, 103066.
57. Yan, K.; Fan, Y.; Hu, F.; et al. A "Polymer-in-Salt" Solid Electrolyte Enabled by Fast Phase Transition Route for Stable Zn Batteries. *Adv. Funct. Mater.* **2024**, *34*, 2307740.
58. Lv, Z.; Kang, Y.; Chen, J.; et al. Stable Solid-State Zinc–Iodine Batteries Enabled by an Inorganic $ZnPS_3$ Solid Electrolyte with Interconnected Zn^{2+} Migration Channels. *Adv. Funct. Mater*. **2024**, 34, 2310476.
59. Zhou, C.; Wang, Z.; Nan, Q.; et al. Simultaneous Inhibition of Vanadium Dissolution and Zinc Dendrites by Mineral-Derived Solid-State Electrolyte for High-Performance Zinc Metal Batteries. *Angew. Chem. Int. Ed.* **2024**, *136*, e202412006.
60. Chen, Z.; Huang, Z.; Wang, C.; et al. Supramolecular Crystals based Fast Single Ion Conductor for Long-Cycling Solid Zinc Batteries. *Angew. Chem. Int. Ed*. **2024**, *63*, e202406683.